12th International Symposium on Applications of Laser Techniques to Fluid Mechanics
Lisbon, Portugal, July 12-15, 2004

Studies of Hydroxyl Distribution and Soot Formation in Turbulent Spray Flames

James R. Gord,[1] Terrence R. Meyer,[2] Sukesh Roy,[2] Sivaram P. Gogineni[2]

[1]Air Force Research Laboratory, Propulsion Directorate
Wright-Patterson Air Force Base, OH 45433-7103, USA

[2]Innovative Scientific Solutions, Inc.
2766 Indian Ripple Road, Dayton, OH 45440-3638, USA

Abstract

A measurement system that combines several laser-based imaging techniques is developed for characterizing the instantaneous flame structure and soot-formation mechanisms in an atmospheric-pressure, swirl-stabilized, liquid-fueled, model gas-turbine combustor. Planar laser-induced incandescence (LII) is used to map the soot volume fraction and planar laser-induced fluorescence (PLIF) of the hydroxyl radical (OH) is used to image the flame zone. Mie scattering, which appears as an interference in the OH PLIF signal, is used to a limited extent as a spray diagnostic. Optimal excitation and detection parameters to enable the simultaneous use of these techniques in turbulent spray flames are discussed, along with analyses of potential sources of error. The data indicate that the flame in the near field of the swirl-stabilized injector is highly perturbed by large-scale structures and that fluid-flame interactions have a significant impact on soot formation. Rich pockets of fuel and air along the interface between the spray flame and recirculation zone serve as locations for soot inception, as shown below (left). The effect of local equivalence ratio is determined from qualitative analysis of the OH-PLIF data and comparison with equilibrium calculations in the recirculation region. Spatially averaged LII measurements demonstrate that soot volume fraction in the primary flame zone increases exponentially with equivalence ratio. This is illustrated in the semi-log plot shown below (right) for two different jet fuels. Preliminary results suggest that soot formation in the primary zone is strongly dependent on fuel aromatic content.

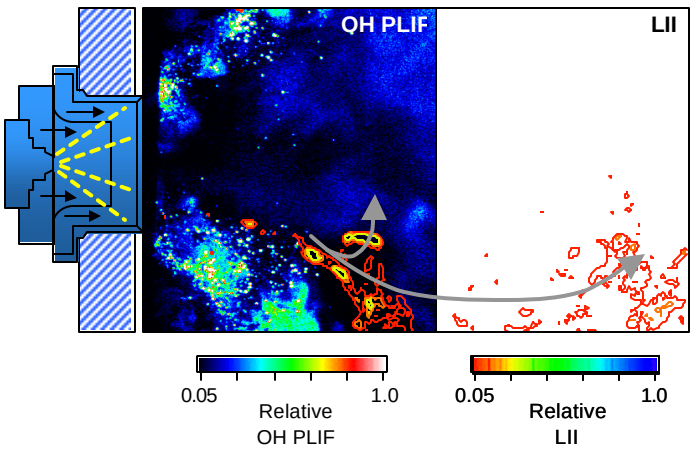

Simultaneous OH-PLIF (left half) and laser-induced incandescence (full image) at overall equivalence ratio of 1.0 for JP-8-fueled, swirl-stabilized spray flame.

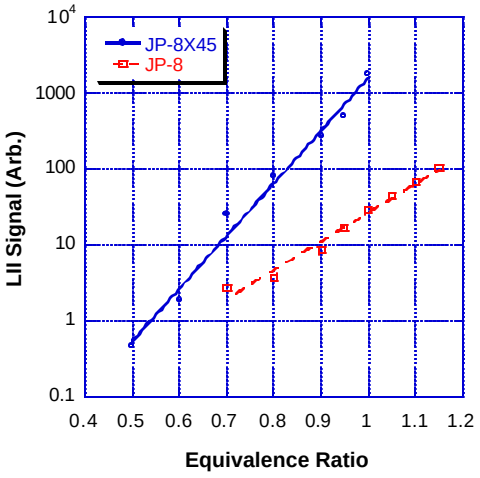

Comparison of relative soot-volume fraction as a function of equivalence ratio for two different jet fuels.

1. Introduction

Swirl-stabilized, liquid-spray injectors are commonly used in gas-turbine engines to achieve compact, stable, and efficient combustion. The flowfield in the primary zone of such a spray flame is characterized by high shear stresses and turbulent intensities that result in vortex breakdown and large-scale unsteady motions.[1,2] These unsteady motions are known to play a key role in the formation of pollutant emissions such as carbon monoxide (CO), nitric oxide (NO), and unburned hydrocarbons (UHC).[3-5] Considerably less is known, however, about the mechanisms that lead to soot formation in swirl-stabilized, liquid-fueled combustors. Previous investigations have relied on exhaust-gas measurements and parametric studies to gain insight into the effects of various input conditions on soot loading.[6-10] Much of the fundamental knowledge concerning soot formation is derived from investigations of laminar diffusion flames,[11,12] with only a limited number of studies having focused on unsteady effects.[13,14] The importance of considering unsteadiness and fluid-flame interactions was demonstrated by Shaddix et al.,[14] who found that a forced methane/air diffusion flame produced a four-fold increase in soot volume fraction (as a result of increased particle size) as compared with a steady flame having the same mean fuel-flow velocity.

The goal of the current investigation is to study soot formation in the highly dynamic environment of a swirl-stabilized, liquid-fueled combustor. This is accomplished using simultaneous imaging of the soot volume fraction, hydroxyl-radical (OH) distribution, and droplet pattern in the primary reaction zone using laser-induced incandescence (LII), OH planar laser-induced fluorescence (PLIF), and droplet Mie scattering, respectively. The utility of LII for two-dimensional imaging of soot volume fraction has been demonstrated in laboratory investigations[15,16] as well as in aircraft-engine exhausts.[9,10] Brown et al.[17] performed planar LII for soot-volume-fraction imaging in the reaction zone of a gas-turbine combustor; their preliminary measurements employed LII alone for demonstration purposes and did not image the turbulent flame structure near the exit of the swirl cup. In the current work, we extend the work of Brown et al.[17] by performing LII at the exit of the swirl cup and by adding OH-PLIF and Mie scattering diagnostics.

The use of OH as a flame marker is typical in studies of soot formation in diffusion flames because of its close correlation with flame temperature.[18,19] It has also been employed in a number of investigations of swirl-stabilized combustors.[20,21] The use of laser-saturated OH LIF for *quantitative* measurements has also been demonstrated, [22,23] although saturation is quite difficult in the case of planar measurements. In the current investigation, we demonstrate qualitative measurements in the recirculation region using excitation levels well below saturation. OH-PLIF measurements in the liquid-spray region are more uncertain because of simultaneous droplet scattering and non-equilibrium conditions, although meaningful measurements are possible with careful consideration of potential errors.

The performance and accuracy of the planar LII, OH-PLIF, and Mie scattering systems are characterized in the current work and described below. The combined use of LII, OH PLIF, and droplet Mie scattering is then shown to provide insight into the unsteady physical processes that govern soot formation in gas turbine engines. OH PLIF is employed to track local equivalence ratio and the effects of flame chemistry. Finally, the current measurement system is demonstrated to be useful in assessing the performance soot-mitigating additives.

2. Experimental Setup

2.1 Swirl-Stabilized Combustor

The near-field structure of swirl-stabilized flames is determined by the characteristics of the fuel injector and the geometry of the surrounding flame tube. As shown in Fig. 1, the swirl-cup, liquid-fuel injector used in the current study employs pressure atomization and dual-radial, counter-swirling-air co-flows to entrain the fuel, promote droplet break-up, and enhance mixing. The 4.3-cm-exit-diameter swirl cup is installed at the entrance of a 15.25-cm × 15.25-cm square-cross-section flame tube, as shown in Fig. 2. After exiting the primary flame zone, the combustion products are allowed to mix thoroughly along the 48-cm long flame tube before entering a 43-cm-long, 5.7-cm-exit-diameter exhaust nozzle that is designed to create uniform exhaust-gas-temperature and concentration profiles.

The combustor shown in Fig. 2 is used in the Atmospheric-Pressure Combustor-Research Complex of the Air Force Research Laboratory's Propulsion Directorate to study the performance characteristics of model gas-turbine-engine fuels and fuel additives. An overview of the facility is available in the literature,[25] although certain aspects relevant to the current work are described here for reference. Changes in overall equivalence ratio from ϕ = 0.5 to 1.15 are achieved in the current study by varying the pressure drop across the fuel-spray nozzle from about 1.5 to 10 atm, which results in fuel mass-flow rates of 1.0 to 2.2 g/s, respectively. The fuel flow rate is measured using a Max Machinery positive-displacement flow meter with ±0.5% full-scale accuracy. The air-flow system consists of three Sierra 5600 SLPM mass-flow controllers with ±1% full-scale accuracy. The inlet air is heated to 450 K with a constant flow rate of ~0.028 kg/s. The air-pressure drop across the combustor dome is ~4.8 to 5.2% of the main supply. Most of the air flow enters the combustor through the swirl-cup injector, but a small percentage enters through aspiration holes along the aft wall. No liner air jets are used in the secondary zone; therefore, the fuel-air ratio depends almost entirely on the flow rates through the injector cup.

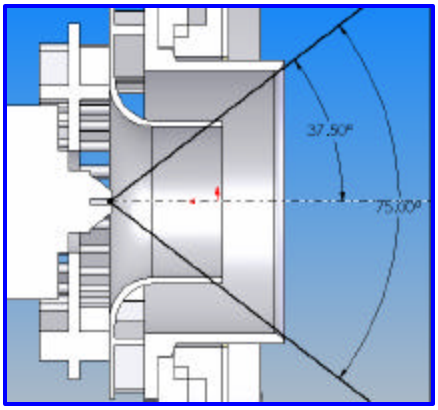

Fig. 1. Center-mounted swirl injector with dual-air counterswirlers.

The combustor is optically accessible via 75-mm-wide quartz windows along the top and sides for *in-situ*, laser-based diagnostics. In addition, a sampling probe for measuring particle number density (counts per cubic centimeter) via a condensation nuclei counter (CNC) is located at the exit of the combustor.

2.2. OH-PLIF System

A review of PLIF fundamentals can be found in Eckbreth (1996).[26] As shown in the optical set-up in Fig. 2, 50% of the laser energy from a frequency-doubled, Q-switched Nd:YAG laser (Spectra-Physics Pro290) is used to pump a dye laser (Sirah Precision Scan), the output of which is frequency doubled to obtain wavelenghts in the (1,0) band of the OH A-X system. The dye laser is tuned to the $Q_1(9)$ transition at 283.922 nm (in air), which has less than ±2.5% variation in the ground-level Boltzmann fraction from 1600 to 2400 K. As shown in Fig. 3, this range of temperatures coincides with the equilibrium conditions expected for JP-8 fuel at equivalence ratios used in this study (ϕ = 0.5 to 1.15).[27] Considering the full range of temperatures from 1100 to 2400 K, which are within typical lean and rich flammability limits,[28] the Boltzmann fraction for this transition varies by up to ±12.5%.

The maximum laser energy available for OH PLIF is 24 mJ. A 1.5-m-focal-length spherical plano-convex lens and a -75-mm-focal-length plano-concave lens are used to form a laser sheet that enters the combustor through the top window. The laser-sheet thickness is 330 µm at full-thickness-half-max (FTHM) as measured by translating a knife edge across the beam. A 7-cm, top-hat-like sheet-width profile that transitions to zero laser energy within about 1 mm is obtained by clipping the wings of the laser sheet at the last turning mirror above the combustor. The sheet is slowly expanding with a 3° full-angle divergence.

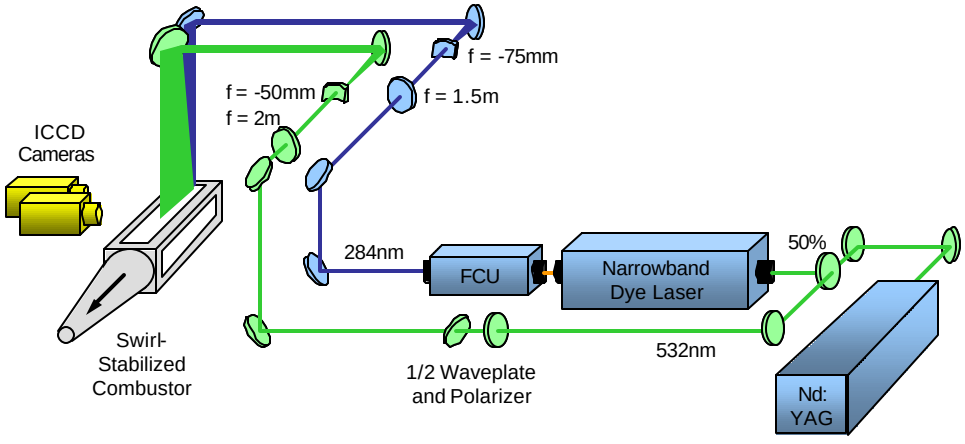

Fig. 2. Optical set up for simultaneous OH PLIF and LII.

Fluorescence is collected from about 306 to 320 nm via the (1,1)

and (0,0) bands of OH using an intensified charge-coupled-device (ICCD) camera (Princeton Instruments PI-MAX SB) oriented slightly off-normal to the sheet. Two 1-mm WG295 Schott Glass filters are used in front of the camera lens to reduce scattering from droplets at 283.922 nm. A UG11 filter nearly eliminates flame emission, scattering from the LII laser at 532 nm, and fluorescence from polycyclic aromatic hydrocarbons (PAH's). A 105-mm-focal-length f/4.5 UV lens is used to collect the OH fluorescence. An intensifier gate width of 20 ns is used to capture the OH signal. Images are typically collected with 2x2 binning (512×512) to obtain adequate resolution and framing rate. The pixel viewing area in each 2x2 superpixel is 200×200 μm^2. Table 1 summarizes the OH-PLIF optical parameters.

Based on the dimensions of the OH-PLIF laser sheet and total available laser energy of 24 mJ, it is estimated that the maximum laser irradiance of 1.36×10^7 W/cm^2 is two to three orders of magnitude lower than that required to achieve 90-95% saturation.[22,23] The OH-PLIF signal is, therefore, linearly related to laser-energy variations. OH-PLIF signal corrections (typ. ±15%) in the axial direction are performed in post processing, based on measurements of the laser-sheet profile after each run. Signal variation (typ. ±3%) due to the 3° laser-sheet expansion in the cross-stream direction is also corrected in post processing. Corrections are not made for laser-energy attenuation due to OH absorption and droplet scattering; this leads to signal uncertainties of ±10% in the lower region of each image. The effect of this error is substantially reduced in the upper half of the combustor, where most of the data in this study is extracted. Shot-to-shot fluctuations in laser energy add an estimated ±5% uncertainty, as determined from data collected in a laminar diffusion flame with the same OH-PLIF system.

For measurements with low laser irradiance, the effect of collisional quenching on fluorescence efficiency must also be considered. For a given imaging system and laser irradiance, the OH-PLIF signal, S_{OH}, from each pixel volume is proportional to the OH number density, N_{OH}, and the fluorescence efficiency, h,[26] as shown in Eqn. 1.

$$S_{OH} \approx N_{OH} h = N_{OH} \frac{A_{OH}}{A_{OH} + Q_{OH}} \tag{1}$$

The fluorescence efficiency is proportional to the rate of spontaneous emission, A_{OH}, from molecules in the excited state and inversely proportional to the rate at which excited molecules are depleted via spontaneous emission and collisional quenching, Q_{OH}. Collisional quenching is a function of the temperature- and pressure-dependent quenching coefficient as well as the number densities of the quenching species.[29] As a result of offsetting effects in the equilibrium combustion products of JP-8, the collisional quenching rate is found to be fairly constant for equivalence ratios less than unity, as shown in Fig. 3. Under rich conditions the conversion of CO to CO_2 decreases substantially, leading to an increase in collisional quenching and a decrease in fluorescence efficiency. In regions where equilibrium assumptions are valid, the LIF signal can be used along with Eqn. 1 and the Boltzmann distribution to determine the relative OH number density; this will be discussed further in the Results Section. In the liquid-spray region where lean and rich pockets co-exist, qualitative signal interpretation is problematic since signal efficiency can vary by more than ±30%, according to Fig. 3.

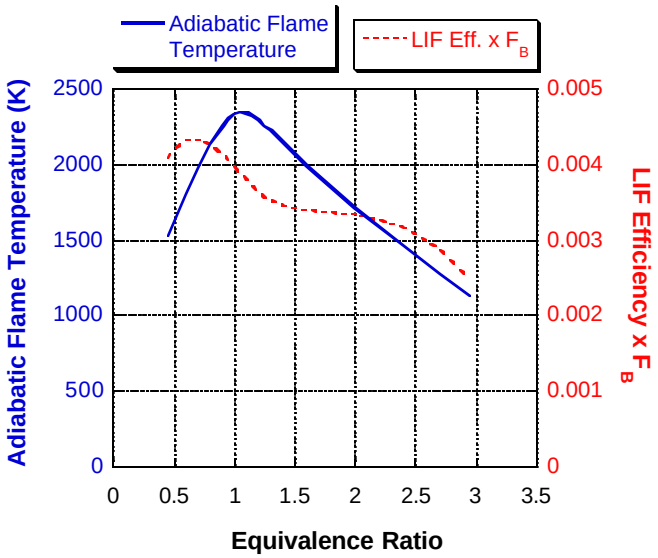

Fig. 3. Adiabatic-flame-temperature calculations assuming equilibrium combustion products along with OH-LIF efficiency multiplied by the Boltzmann fraction for JP-8 fuel at various equivalence ratios.

Mie scattering is obtained using the same optical setup as that for the OH-PLIF system. It is found that optical filters and the use of parallel polarization in the detection scheme can reduce but not altogether eliminate droplet scattering. It is found that two WG295 color-glass filters (CVI Laser) and parallel-polarization detection provide optimal OH-PLIF sensitivity while minimizing

the likelihood of damaging the ICCD due to intense levels of droplet scattering. When the laser is tuned off the OH absorption line, as shown in Fig. 4, the intense, highly localized droplet scatter can be distinguished from the large, more uniformly distributed OH layers. Large droplet clusters appear primarily near the injector exit, and single droplets with trailing flames are often observed traveling into the recirculation region. The trailing flames of these droplets do not appear in the off-line images and, therefore, are not attributable to scattering from fuel vapor or fluorescence from broadband sources such as PAH compounds. The droplet-scattering signal intensity is about one order of magnitude higher than that of the OH PLIF, but the signal occurs primarily at isolated points. A false-color table is selected, therefore, based on probability density functions of OH PLIF. The full range of OH-PLIF signal levels is assigned colors from black to red, while the Mie scattering signals are above this range and appear in white.

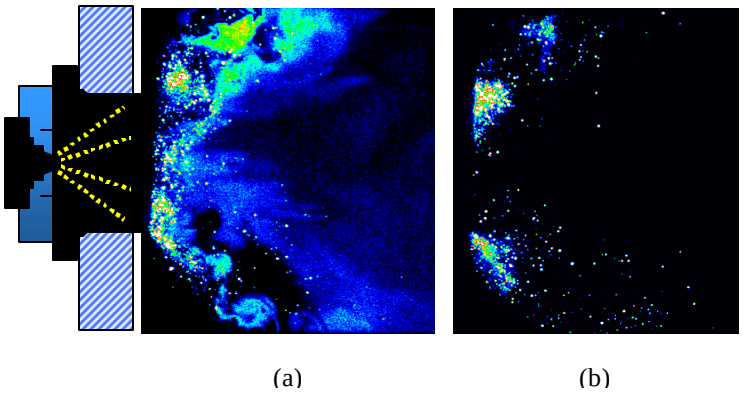

Fig. 4. Raw signal from (a) OH PLIF and droplet Mie scattering while on $Q_1(9)$ line of (1,0) band in A-X system and (b) droplet Mie scattering while off the OH line. Overall f = 0.7.

2.3. LII System

Some of the first two-dimensional visualizations of soot volume fraction using LII were performed by Santoro and co-workers[15] and by Vander Wal and Weiland.[16] The effects of various parameters such as laser fluence, laser-sheet profile, detection wavelength, camera gate width, and camera gate delay have been explored in a number of follow-up investigations.[30-32] A list of reviews on the subject is provided by Urban.[12]

The LII optical layout employed in the current study is shown schematically in Fig. 2, where 50% of the energy from a frequency-doubled Nd:YAG is formed into a sheet using a 2-m plano-convex spherical lens and a -50-mm plano-concave cylindrical lens. The FTHM of the laser sheet is about 700 μm within the measurement volume, as measured by traversing a knife edge across the sheet. As is the case for the OH-PLIF laser sheet, the long 2-m-focal-length lens is used to minimize variations in laser-sheet thickness within the measured region. The sheet width is ~14 cm, with wings that are clipped prior to the last turning mirror to generate a top-hat-like profile that transitions to zero laser energy within about 2 mm. The sheet has a full angle divergence of 6° within the test section. An overall tilt of 5° is used to overlap the LII and PLIF laser sheets. The laser-fluence distribution varies by ±15% over the first 7 cm of the sheet, corresponding to the region where PLIF and Mie scattering are measured. Over the remaining 7 cm of the sheet, the laser fluence decreases more quickly from a peak of 460 mJ/cm^2 to a minimum of 180 mJ/cm^2. To reduce systematic errors due to laser-sheet-width intensity variations in the downstream half of the laser sheet and due to laser extinction in the measurement volume, the LII system is operated in the saturated regime. A saturation fluence near 200 mJ/cm^2, shown in Fig. 5, agrees with previous measurements in the literature.[30,32] Figure 5 indicates that the uncertainty in the relative soot-volume-fraction measurements is within ±10% over the full width of the laser sheet.

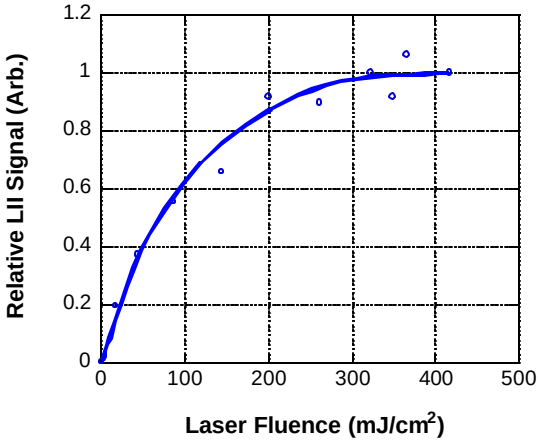

Fig. 5. LII saturation curve from averaged images in a swirl-stabilized combustor at overall f = 1.1. Solid line is for guidance only.

The LII signal is detected using a 1024×1024 ICCD camera (Princeton Instruments PI-MAX SB-MG) and an f/1.2, 58-mm-focal-length glass lens. After 4x4 pixel binning, the measurement resolution is about 575×575 μm^2. A 500-nm

Table 1. Summary of OH-PLIF optical parameters for optimal detection in the primary flame zone.

	OH-PLIF Parameter	Criteria
Camera gate width	20 ns	Minimize flame emission
Camera delay	0 ns	Maximize signal
Excitation wavelength	283.922 nm	Temperature insensitivity
Detection wavelength	306 - 320 nm	Minimize scatter and flame emission
Length of meas. volume	2.5”	Visualize primary flame zone
Thickness of meas. volume	330 mm	High resolution and laser fluence
Laser fluence	30 - 40 mJ/cm^2	Maximize signal

Table 2. Summary of LII optical parameters for optimal detection in the primary flame zone.

	LII Parameter	Criteria
Camera gate width	50 ns	Minimize particle-size bias
Camera delay	20 ns	Minimize scatter/ PAH fluorescence
Excitation wavelength	532 nm	Safety and beam quality
Detection wavelength	415 - 500 nm	Minimize PAH and wavelength effects
Length of meas. volume	5”	Visualize primary flame zone & beyond
Thickness of meas. volume	700 mm	Adequate resolution and meas. volume
Laser fluence	200 - 420 mJ/cm^2	Saturate signal

short-pass filter (CVI Laser) is used for detection from 415 to 500 nm, which reduces contributions from nascent soot particles, OH fluorescence/chemiluminescence, and red-shifted fluorescence from PAH compounds. The relatively short-lived PAH fluorescence is also minimized by employing a time-delayed detection scheme. Scattering from the 532-nm laser source is eliminated by using a 532-nm zero-degree reflective mirror with the 500-nm short-pass filter and delayed detection. Light leakage from flame luminosity while the ICCD intensifier is gated off is minimized through the use of a 25-ms-gate Uniblitz shutter. During post processing the residual background signal from flame luminosity is subtracted from each image. A color scale is chosen with a minimum value 5% above the background and a maximum value at 100% signal.

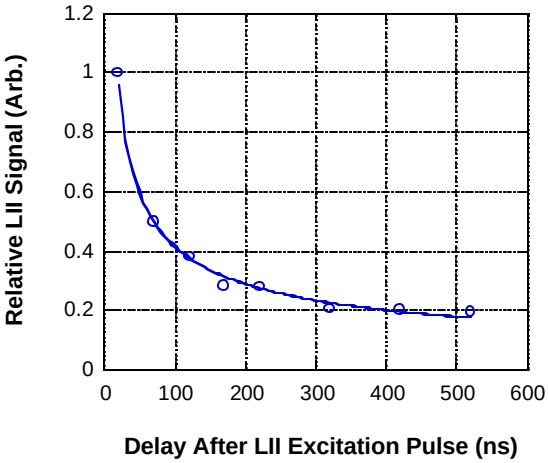

Fig. 6. Power-law time dependence of LII signal in swirl-stabilized combustor at ϕ = 1.1.

To optimize the timing of LII detection, data are collected in the swirl-stabilized flame for a number of camera-intensifier-gate delays and widths. A camera delay of 20 ns after the laser pulse is found to reduce laser scatter to nearly the background level while maintaining LII signal-to-noise ratios greater than 20:1. The LII signal decays quickly within the first 200 ns after the laser pulse, as shown in Fig. 6. The long decay in signal after 200 ns is dominated by larger, slow-cooling particles. With a gate width of 50 ns, errors due to particle-size effects are estimated to be on the order of 5-10%.[30] Table 2 summarizes the optical parameters used for LII.

2.4. Combined LIF/LII System

The OH-PLIF and LII cameras are synchronized using an external delay generator (Stanford Research Systems DG535) driven by the advanced Q-switch TTL output of the Nd:YAG laser. The laser pulses are separated by only a few nanoseconds to avoid fluid movement during LIF and LII detection. The precise camera delay required to capture each image is imposed using a timing generator in each ICCD controller. Because of spatial constraints within the test cell, both cameras are positioned on the same side of the combustor at 3.5° to normal to overlap the two imaged regions. This angle is minimized by placing the LIF image to the far right of the camera viewing area and using a relatively large LII viewing area. Thus, the PLIF image area overlaps the left half of the LII image nearest the injector cup. After camera alignment, registration images are collected prior to each run for use in post processing. At higher equivalence ratios (>0.7), thermal loading from flame radiation is significant, and heat shielding is employed to reduce misalignment of the LII/LIF optics. During each run the OH-PLIF and LII sheets are checked periodically using burn paper and adjusted to ensure that the laser-intensity distributions and positions have not changed.

3. Results and Discussion

3.1. Instantaneous Flame Structure

The average OH distribution at ϕ = 0.5 is shown in Fig. 7(a). All images are background subtracted and corrected for laser-sheet intensity variations and laser-sheet divergence. A slight asymmetry is apparent in the upper and lower halves, with the effects of laser attenuation being evident in the lower half of the image.

The intermittency and spatial inhomogeneity of the instantaneous flame structure is shown by the OH-PLIF images in Figs. 7(b) and 7(c). These images indicate that the fuel-preheat and reactant-mixing layers are highly turbulent. The instantaneous thickness of the OH layer varies significantly because of fluid entrainment from large-scale vortex structures. These structures are shed from the shear layer that is anchored on the lip of the outer air swirler; they enhance the mixing process, bring fresh reactants into the outer conical flame, and can reach across the flame layer and be a source of local flame extinction and intermittency. The latter is more prominent in Fig. 7(c), which shows an instantaneous OH-PLIF image at ϕ = 0.9 with no contiguous flame in the viewing area. The size of the

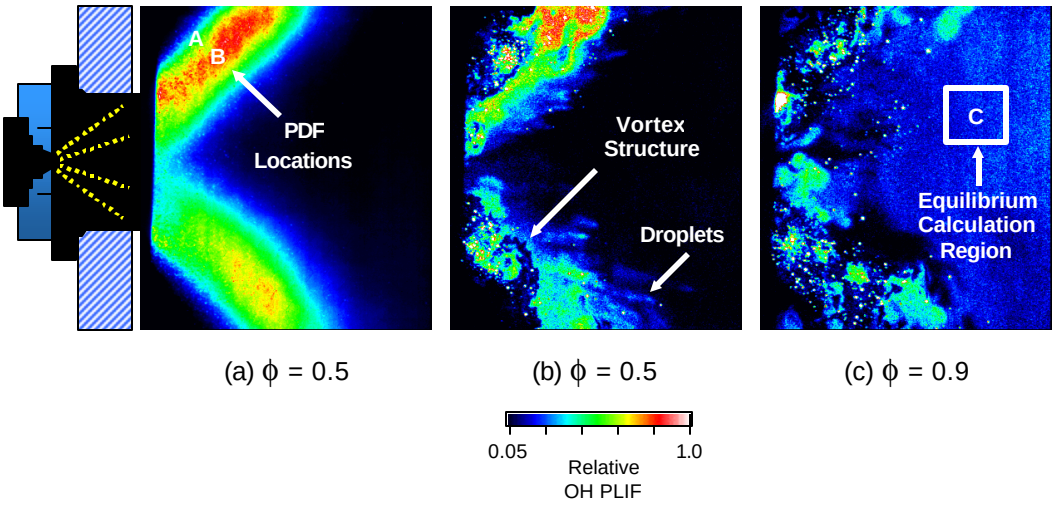

Fig. 7. Post-processed OH-PLIF images: (a) time-averaged image at overall f = 0.5, (b) instantaneous image at overall f = 0.5, and (c) instantaneous image at overall f = 0.9. Horizontal and vertical extent of signal is 4 to 70 mm from injector exit and -39 to 39 mm from injector centerline, respectively.

structures in Figs. 7(b) and 7(c) that are generated during the turbulent cascade from large to small scales ranges from about 0.5 mm to the entire width of the flame layer. Since the air-flow rate is held constant, much of this intermittency can be attributed to the behavior of the liquid spray as it impinges upon and sheds off the lip of the outer air swirler. This indicates that experiments and computations based on gaseous-fuel injection would not capture the significant changes in large-scale-structure dynamics induced by increased liquid-fuel injection.

To quantify the intermittency of the primary flame layer, probability density functions (PDF's) of OH PLIF signals are computed and plotted in Fig. 8 for Locations A and B shown in Fig. 7(a). Bin sizes of 200 counts are used along with 200 images. Normalization is performed only for data in the range 0 - 6000 counts, which is below the range typically observed from droplet Mie scattering. Location A is within the mixing layer dominated by large-scale turbulent structures, while Location B is within the central region of the outer conical flame. The PDF's at both locations show bimodal distributions but with opposite peaks. At Location A high levels of intermittency lead to a primary peak with low signal counts and a secondary peak with 3000-3500 counts. At Location B low-signal counts have decreased in probability and high-signal counts have increased in probability, indicating that large-scale structures seldom bring fresh reactants to this point in the flame at $\phi = 0.5$.

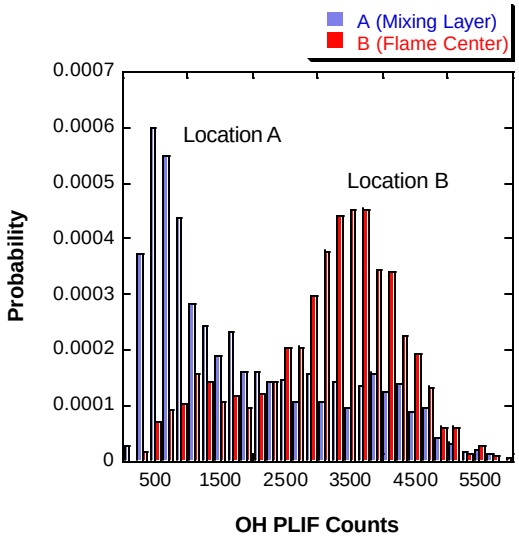

Fig. 8. Probability density functions (PDF's) of the corrected OH-PLIF signal at Location A (mixing layer) and Location B (flame center) shown in the average image of Fig. 7(a).

3.2. Determination of Local Equivalence Ratio

Figures 7(b) and 7(c) also show the distribution of droplets marked by Mie scattering. This signal, which scales as the droplet diameter squared, is biased toward larger droplets and cannot be used to interpret the true size distribution. However, it can be used as a qualitative marker for those large droplets that escape the initial preheat zone. Interestingly, the droplets in Fig. 7(b) have trailing flames, which indicates that evaporation and mixing with available oxygen is occurring in their wakes. Figure 7(c), however, shows droplets entering the recirculation zone without trailing flames. Since the temperature, evaporation, and reaction rates are expected to be higher in this

region for the higher equivalence ratio of Fig. 7(c), the absence of trailing flames indicates a lack of available oxygen for combustion. This is somewhat surprising since the combustor is operating at *overall* lean equivalence ratios in both Figs. 7(b) and 7(c).

In fact, it can be shown that the *local* equivalence ratio for the case of Fig. 7(c) is higher than the *overall* value of 0.9. Using a region in the recirculation zone that is free of droplet scatter [see Fig. 7(c)], an equilibrium calculation[27] is performed for JP-8 fuel at equivalence ratios varying from 0.5 to 1.15. The validity of equilibrium assumptions in this region has been proposed in previous investigations of can-type gas-turbine combustors.[3,4] The temperatures and species concentrations from this equilibrium calculation are then used to calculate the effects of LIF efficiency and Boltzmann fraction on OH-PLIF signals, as shown previously in Fig. 3. The fit of OH-PLIF signals to equilibrium calculations, shown in Fig. 9, indicates that the local equivalence ratio is 13.5% higher than the overall equivalence ratio. Thus, the stoichiometric condition in the primary flame zone occurs for *overall* equivalence ratios between 0.8 and 0.9. Correspondingly, images collected at these equivalence ratios show a transition from burning to non-burning wakes behind droplets. The occurrence of locally rich conditions near the primary flame zone may be due in part to air from the aspiration holes of the aft wall escaping the primary flame zone or due to incomplete mixing in the flame recirculation region. The significance of this finding for understanding soot formation mechanisms and evaluating differences with sampling-probe data in the exhaust stream are discussed below.

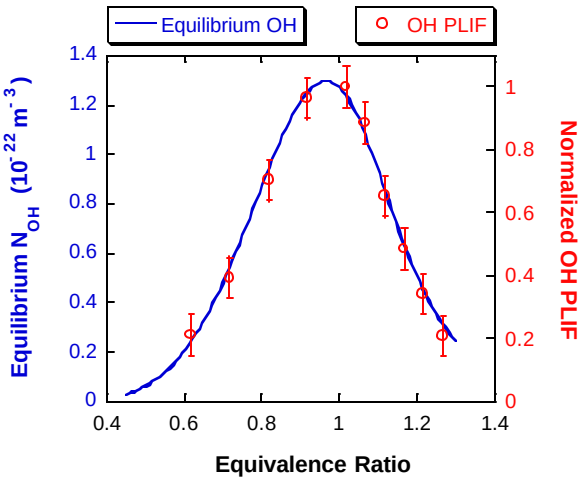

Fig. 9. Theoretical OH number density compared with OH-PLIF data in the recirculation zone [Region C in Fig. 7(c)]. OH-PLIF data are corrected for variations in fluorescence efficiency and Boltzmann fraction with f (see Fig. 3).

3.3. Soot-Formation Mechanisms

Figure 10 shows two instantaneous LII contour plots at $\phi = 1.0$ overlayed with OH-PLIF images that are collected simultaneously. It should be noted that these LII images are typical for about 5% of the data set. More commonly, the spatial extent of the LII signal from highly concentrated soot pockets encompasses less than 1% of the primary flame zone. Images such as those in Fig. 10, therefore, account for the "turbulent flame brush" that may be responsible for most of the soot production in liquid-spray flames. The flow patterns noted in the figure are derived using observations from high-speed digital images collected in the same combustor. Soot is generated along the inner cone of the flame in regions of low OH-PLIF intensity. A portion of the soot is advected along the outer path of the recirculation zone, while a portion appears to enter immediately into the recirculation zone.

Most of the LII signal is detected in regions that are free of droplet Mie scattering (as detected with the OH-PLIF camera) and is attributable to the presence of soot. Some of the LII signal does occur in regions of high Mie scattering, indicating that some, if not most, of the signal near the injector exit cannot be attributed to the presence of soot. The LII signal is not likely to come from PAH fluorescence, which should occur prior to the 20-ns gate delay and would appear more consistently near the spray region.

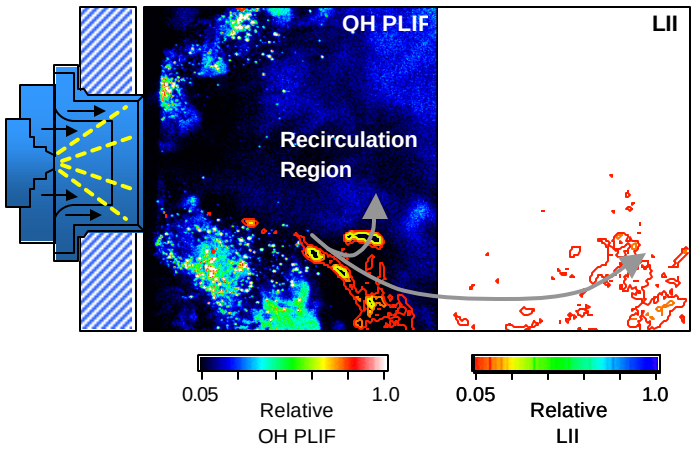

Fig. 10. Simultaneous OH PLIF (left half) and laser-induced incandescence (full image) at overall equivalence ratio of 1.0.

Background images collected without the laser sheet show that the contribution from nascent soot incandescence is less than 5%.

Thus, it is likely that soot formation is, in fact, initiated along the downstream region of the conical flame adjacent to the recirculation zone. The absence of OH PLIF in this region is quite evident in the lower half of the spray flame at low and high overall equivalence ratios [see Fig. 7(c) at $\phi = 0.9$], regardless of whether LII is detected. This region likely contains a rich mixture of fuel and air that escapes the main spray cone because of turbulent interactions. At low overall equivalence ratios [see Fig. 7(b) at $\phi = 0.9$], soot formed within this rich mixture may be oxidized by oxygen and hydroxyl radicals before entering the recirculation zone. At high equivalence ratios, soot formation is aided both by a drop in temperature and by the lack of an oxidizing partner. The soot formed in Region B is advected either downstream or into the recirculation zone.

3.4. Averaged Soot-Volume-Fraction Measurements

The combined use of planar LII, OH PLIF, and Mie scattering has been shown above to provide physical insight into soot formation in the current flame environment. Data described in the discussion that follows demonstrate the utility of LII and OH PLIF for studying the effects of fuel-inlet conditions on soot production. This is illustrated in Fig. 11, where the temporally and spatially averaged relative soot volume fraction is plotted as a function of overall equivalence ratio for the current spray flame. The LII data show an exponential increase in soot volume fraction with equivalence ratio. The sampling probe CNC data display a threshold effect at about $\phi = 1.0$, below which soot in the exhaust is effectively oxidized due to long residence times and greater quantities of O_2 and OH. In the primary zone of the combustor, there is less time to oxidize the soot. In addition, the local ϕ is higher in the primary zone than in the exhaust.

The LII experiment is also performed at two camera gate widths to assess the sensitivity of the data to particle-size effects. A bias toward higher particle sizes for the longer gate duration of 200 ns would be expected. Because of normalization, this bias appears as a slight decrease in signal at lower equivalence ratios for which particle sizes are expected to be smaller. This effect appears to be minimal in Fig. 11 (to within experimental uncertainty), suggesting that detection with a 50-ns gate is also free of significant particle-size effects.

The current measurement system is presently being used to study the effects of particulate-mitigating additives and varying fuel type on soot formation in swirl-stabilized combustors. Figure 12, for example, shows a comparison of the relative soot volume fraction for JP-8 and JP-8X45 (45% aromatic content). The JP-8 data from Fig. 11 are rescaled to that of JP-8X45 to allow a comparison on a semi-log plot. Both show an exponential increase with equivalence ratio, with the soot volume fraction of JP-8X45 varying between one to two orders of magnitude higher in the primary flame zone than that of JP-8.

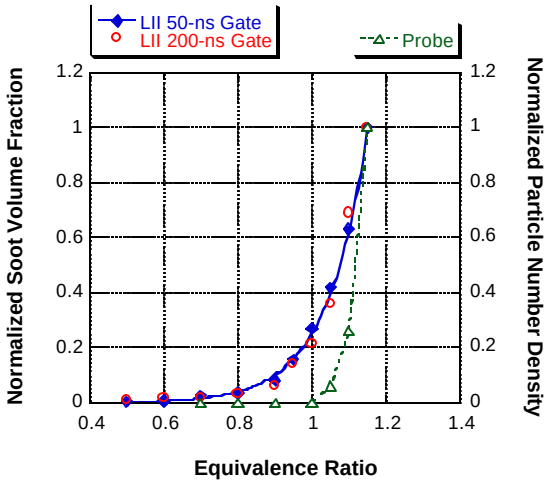

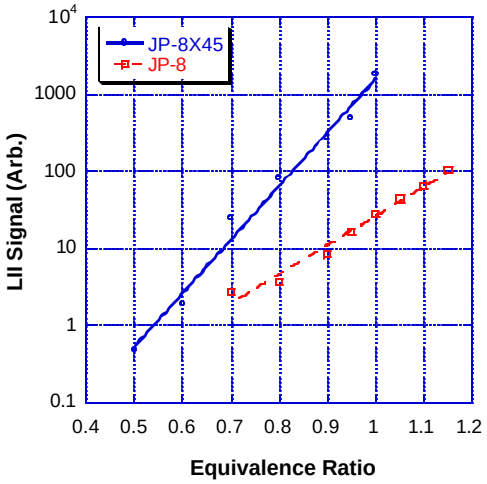

Fig. 12. Relative soot volume fraction for two different jet fuels.

4. Conclusions

A simultaneous planar LII, OH-PLIF, and Mie-scattering system is developed, tested, and demonstrated in a JP-8-fueled, liquid-spray, swirl-stabilized combustor. These combined diagnostics permit phenomenological characterization of soot-formation mechanisms in this highly turbulent environment by mapping the soot volume fraction, instantaneous flame zone, and fuel-droplet behavior. It is found that large-scale structures play a key role in flame intermittency and that soot formation is a strong function of spray-flame interactions as well as local equivalence ratio. Experimental and numerical studies in gaseous-fueled combustors may not capture these dynamics properly. Soot formation in the inner conical flame region correlates with regions of low OH PLIF and droplet Mie scattering. A qualitative study of equivalence-ratio effects on the OH-PLIF signals shows that equilibrium assumptions can be used for OH-signal correction in the recirculation zone. LII data indicate an exponential dependence on equivalence ratio with a strong dependence on fuel aromatic content. Future work includes a broader survey of fuel additives and fuel types.

Acknowledgments

We thank Dr. Vincent Belovich, Dr. Edwin Corporan, Dr. Matthew DeWitt, Dr. Viswanath Katta, and Theodore Williams for their technical input, as well as Michael Arstingstall and Charles Frayne for assistance with the combustor facility. Funding for this research was provided by the Air Force Research Laboratory, Propulsion Directorate, Wright-Patterson AFB, under Contract Nos. F33615-00-C-2068, F33615-D-03-M2829, and F33615-00-C-3020, and by the Air Force Office of Scientific Research (Dr. Julian Tishkoff, Program Monitor).

References

1. W.-W. Kim, S. Menon, and H. Mongia, "Large-eddy simulation of a gas turbine combustor flow," Combust. Sci. Technol. **143**, 25-62 (1999).
2. S. Wang, S.-Y. Hsieh, and V. Yang, "Numerical simulation of gas turbine swirl-stabilized injector dynamics," AIAA paper 2001-0334 (American Institute of Aeronautics and Astronautics, Reston, VA, 2001).
3. M. V. Heitor, and J. H. Whitelaw, "Velocity, Temperature, and Species Characteristics of the Flow in a Gas-Turbine Combustor," Combust. Flame **64**, 1-32 (1986).
4. A. F. Bicen, D. G. N. Tse, and J. H. Whitelaw, "Combustion Characteristics of a Model Can-Type Combustor," Combust. Flame **80**, 111-125 (1990).
5. T. J. Held, M. A. Mueller, S.-C. Li, and H. Mongia, "Data-driven model for NO_x, CO and UHC emissions for a dry low emissions gas turbine combustor," AIAA paper 2001-3425 (American Institute of Aeronautics and Astronautics, Reston, VA, 2001).
6. W. A. Eckerle, "Soot loading in a generic gas turbine combustor," AIAA paper 87-0297 (American Institute of Aeronautics and Astronautics, New York, NY, 1987).
7. T. C. Fang, C. M. Megaridis, W. A. Sowa, and G. S. Samuelsen, "Soot morphology in a liquid-fueled swirl-stabilized combustor," Combust. Flame **112**, 312-328 (1998).
8. D. R. Snelling, K. A. Thomson, G. J. Smallwood, and O. L. Gulder, "Two-dimensional imaging of soot volume fraction in laminar diffusion flames," Appl. Opt. **38**, 2478-1485 (1999).
9. J. D. Black, "Laser Induced Incandescence Measurements of Particles in Aero-Engine Exhausts," SPIE Vol. 3821, EUROPTO Conference on Environmental Sensing and Applications, Munich, Germany (1999).
10. T. P. Jenkins, J. L. Bartholomew, P. A. DeBarber, P. Yang, J. M. Seitzman, and R. P. Howard, "A laser-induced incandescence system for measuring soot flux in aircraft engine exhausts," AIAA paper 2002-3736 (American Institute of Aeronautics and Astronautics, Reston, VA, 2002).
11. R. J. Santoro, T. T. Yeh, J. J. Horvath, and H. G. Semerjian, "The transport and growth of soot particles in laminar diffusion flames," Combust. Sci. Technol. **53**, 89-115 (1987).
12. D. L. Urban and G. M. Faeth, "Soot research in combustion science: introduction and review of current work," AIAA paper 2001-0322 (American Institute of Aeronautics and Astronautics, Reston, VA, 2001).
13. Y.-H. Won, T. Kamimoto, H. Kobayashi, and H. Kosaka, "2-D soot visualization in unsteady spray flame by means of laser sheet scattering technique," SAE Tech. Paper 910223 (Society of Automotive Engineers, Warrendale, PA, 1991).

14. C. R. Shaddix, J. E. Harrington, and K. C. Smyth, "Quantitative Measurements of Enhanced Soot Production in a Flickering Methane / Air Diffusion Flame," Combust. Flame **99**, 723-732 (1994).
15. B. Quay, T.-W. Lee, T. Ni, and R. J. Santoro, "Spatially Resolved Measurements of Soot Volume Fraction Using Laser-Induced Incandescence," Combust. Flame **97**, 384-392 (1994).
16. R. L. Vander Wal and K. J. Weiland, "Laser-induced incandescence: Development and characterization towards a measurement of soot-volume fraction," Appl. Phys. B **59**, 445-452 (1994).
17. M. S. Brown, T. R. Meyer, J. R. Gord, V. M. Belovich, and W. M. Roquemore, "Laser-induced incandescence measurements in the reaction zone of a model gas turbine combustor," AIAA paper 2002-0393 (American Institute of Aeronautics and Astronautics, Reston, VA, 2002).
18. K. C. Smyth, J. H. Miller, R. C. Dorfman, W. G. Mallard, and R. J. Santoro, "Soot inception in a methane/air diffusion flame as characterized by detailed species profiles," Combust. Flame **62**, 157-181 (1985).
19. F. Cignoli, S. Benecchi, and Z. Giorgio, "Simultaneous one-dimensional visualization of OH, polycyclic aromatic hydrocarbons, and soot in a laminar diffusion flame," Opt. Lett. **17**, 229-231 (1992).
20. W.-P. Shih, J. G. Lee, and D. A. Santavicca, "Stability and emissions characteristics of a lean premixed gas turbine combustor," in the Twenty-Sixth Symposium (International) on Combustion (The Combustion Institute, Pittsburg, PA, 1996).
21. R. E. Foglesong, T. R. Frazier, L. M. Flamand, J. E. Peters, and R. P. Lucht, "Flame structure and emissions characteristics of a lean premixed gas turbine combustor," AIAA paper 99-2399 (American Institute of Aeronautics and Astronautics, Reston, VA, 1999).
22. R. P. Lucht, D. W. Sweeney, and N. M. Laurendeau, "Laser-saturated fluorescence measurements of OH concentration in flames," Combust. Flame **50**, 189-205 (1983).
23. C. D. Carter, G. B. King, and N. M. Laurendeau, "Saturated fluorescence measurements of the hydroxyl radical in laminar high-pressure $C_2H_6/O_2/N_2$ flames," Appl. Opt. **31**, 1511-1522 (1992).
24. K. Lee and B. Chehroudi, "Structure of a swirl-stabilized spray flame relevant to gas turbine and furnaces," J. Propul. Power **11**, 1110-1117 (1995).
25. S. Roy, T. R. Meyer, R. P. Lucht, V. M. Belovich, E. Corporan, and J. R. Gord, "Temperature and CO_2-concentration measurements in the exhaust stream of a liquid-fueled combustor using dual-pump coherent anti-Stokes Raman scattering (CARS) spectroscopy," Combust. Flame**,** submitted for publication (2003).
26. A. C. Eckbreth (1996), "Laser diagnostics for combustion temperature and species," 2nd Ed., Gordon and Breach Publishers, The Netherlands.
27. S. R. Turns (1996), "An Introduction to Combustion," McGraw-Hill, New York.
28. A. H. Lefebvre (1999), "Gas turbine combustion," 2nd Ed., Taylor and Francis, Philadelphia, PA.
29. M. Tamura, P. A. Berg, J. Luque, J. E. Harrington, G. P. Smith, J. B. Jeffries, and D. R. Crosley, Combust. Flame **114**, 502-514 (1998).
30. T. Ni, J. A. Pinson, S. Gupta, and R. J. Santoro, "Two-dimensional imaging of soot volume fraction by the use of laser-induced incandescence," Appl. Opt. **34**, 7083-7091 (1995).
31. D. J. Bryce, N. Ladommatos, and H. Zhao, "Quantitative investigation of soot distribution by laser-induced incandescence," Appl. Opt. **39**, 5012-5022 (2000).
32. H. A. Michelsen, "Understanding and predicting the temporal response of laser-induced incandescence from carbonaceous particles," J. Chem. Phys. **118**, 7012-7045 (2003).